Nano Energy 78 (2020) 105368

Contents lists available at ScienceDirect

Nano Energy

journal homepage: http://www.elsevier.com/locate/nanoen

Full paper

# Surface-engineered oxidized two-dimensional Sb for efficient visible light-driven $N_2$ fixation

Zhenqing Zhao [a], Changhyeok Choi [b], Song Hong [c], Huidong Shen [a], Chao Yan [d,**], Justus Masa [e,1], Yousung Jung [b,***], Jieshan Qiu [f], Zhenyu Sun [a,*]

[a] State Key Laboratory of Organic-Inorganic Composites, College of Chemical Engineering, Beijing University of Chemical Technology, Beijing, 100029, China
[b] Department of Chemical and Biomolecular Engineering, Korea Advanced Institute of Science and Technology (KAIST), Daejeon, 34141, Republic of Korea
[c] Analysis Technology R&D Center, Beijing University of Chemical Technology, Beijing, 100029, China
[d] School of Materials Science and Engineering, Jiangsu University of Science and Technology, Zhenjiang, 212003, China
[e] Analytische Chemie-Elektroanalytik & Sensorik, Ruhr University Bochum, D-44780, Bochum, Germany
[f] State Key Laboratory of Chemical Resource Engineering, College of Chemical Engineering, Beijing University of Chemical Technology, Beijing, 100029, China

ARTICLE INFO

*Keywords:*
$N_2$ fixation
Photocatalysis
Two-dimensional Sb
Visible light
Vacancy

ABSTRACT

Solar $N_2$ fixation under visible light offers a promising method toward sustainable $NH_3$ production at benign conditions. However, it still remains a formidable challenge to activate and cleave N≡N bonds and promote the separation and transport of electrons and holes during photocatalysis. To address these issues, the discovery and design of high-performance and robust photocatalysts is imperative. Here, we report the defect engineering of two-dimensional oxidized Sb nanosheets to activate intrinsically inactive Sb for efficient visible light-driven $N_2$ reduction to $NH_3$. Impressively, the Sb nanosheets rich in Sb and oxygen vacancies afford a remarkable $NH_3$ formation rate of up to 388.5 $\mu g_{NH3}\ h^{-1}\ g_{cat.}^{-1}$ without cocatalyst in visible light, 8 times higher than that for bulk Sb and also significantly outperforming many previously reported photocatalysts. The defective Sb nanosheets exhibit excellent stability after five successive reaction cycles. Further density functional theory calculations reveal a considerably strong interaction between $N_2$ and defects on the surface and edge of Sb nanosheets, which facilitates the formation of *NNH ($N_2 + (H^+ + e^-) \rightarrow$ *NNH, where * denotes an adsorption site), thus promoting photocatalytic $N_2$ reduction. This finding opens a novel avenue to enhancing $N_2$ photofixation over inherently inactive surfaces by synergistically engineering defect sites.

## 1. Introduction

Ammonia ($NH_3$), the second most produced chemical in the world after sulfuric acid, is the basis for fertilizers and explosives, and is in general the first product in the nitrogen value chain. $NH_3$ is also considered as an alternative clean and safe fuel. The traditional Haber-Bosch process involving gas-phase reaction between $N_2$ and $H_2$ molecules is still widely employed for industrial $NH_3$ synthesis. However, this method has intrinsic disadvantages such as high energy consumption, extreme reaction conditions (300–500 °C and 15–25 MPa), and excessive emission of $CO_2$, leading to severe environmental issues [1]. Therefore, intensive research presently focuses on the development of clean and environmentally friendly protocols for $N_2$ fixation [2–5].

Photocatalytic $N_2$ reduction using solar energy under ambient conditions provides a green and sustainable strategy for $NH_3$ production [6–11]. Great efforts have been made to explore new semiconductor photocatalysts over the past several decades since the pioneering work on $N_2$ photofixation by Dhar and coworkers over 78 years ago [12–14]. Transition metal-based compounds have been shown to facilitate $N_2$ reduction by accepting lone-pair electrons of $N_2$ molecules to reduce the electron density of their highest occupied molecular orbitals (HOMOs) and back donating *dp* electrons into the anti-binding orbitals to enhance the electron density of their lowest unoccupied molecular orbitals (LUMOs) [15]. Despite recent advances in this field, the overall $N_2$

* Corresponding author.
** Corresponding author.
*** Corresponding author.
*E-mail addresses:* chaoyan@just.edu.cn (C. Yan), ysjn@kaist.ac.kr (Y. Jung), sunzy@mail.buct.edu.cn (Z. Sun).
[1] Current address: Max Planck Institute for Chemical Energy Conversion Stiftstrasse 34–36, 45470 Mülheim an der Ruhr (Germany).

https://doi.org/10.1016/j.nanoen.2020.105368
Received 20 February 2020; Received in revised form 14 August 2020; Accepted 7 September 2020
Available online 10 September 2020

conversion efficiency remains far from satisfactory. Photo-driven $N_2$ reduction still suffers from poor electron transfer from photocatalysts to the antibonding orbitals of $N_2$ to activate the extremely thermodynamically stable N≡N bond [16].

Emerging two-dimensional (2D) materials have gained heightened attention in photocatalysis due to their unique structure and enhanced or novel (electronic and optical) properties when miniaturized to atomic scale thickness [17–19]. 2D nanosheets with a large exposed surface area favour light harvesting, enhance mass transfer, and also inhibit electron and hole recombination by substantially reducing the charge carrier migration distance from the interior to the surface of a semiconductor [20–22]. Equally intriguingly, manipulation of the surface atoms of a 2D structure provides an effective way of tuning its catalytic behaviour. Unlike 2D allotropes of black phosphorus that easily degrade by uptaking moisture from air [23,24], 2D antimony (Sb) is very stable [25] with a bandgap ranging from 0 to 2.28 eV (for a monolayer) [26,27]. The bandgap of Sb starkly contrasts that of the other group 14 elements, including graphene with a zero bandgap [28,29]. These exciting physico-chemical features render 2D Sb an interesting material in photocatalysis. However, reports on photocatalytic $N_2$ fixation by antimony nanosheets are seldom thus far, not to mention the desired sheet-thickness, surface vacancies and their effect on photocatalytic performance.

Herein, we report, for the first time, engineering of 2D oxidized Sb nanosheets with controlled thicknesses and surface vacancy sites to achieve dramatically enhanced $N_2$ photofixation. In sharp contrast to bulk Sb that exhibits poor activity for $N_2$ conversion, the prepared defective Sb nanosheets can efficiently reduce $N_2$ to $NH_3$ under visible light at ambient tempearture and pressure. The $NH_3$ yield rate could be tailored by synergistically manipulating the Sb nanosheet thickness and the nature and density of the defect sites. Moreover, density functional theory calculations show that the Sb and oxygen vacancies on the surface of ultrathin 2D Sb nanosheets play a central role in activating Sb for efficient $N_2$ activation.

## 2. Results and discussion

Owing to the weak van der Waals interactions between layers (Fig. 1a and b), directly exfoliating bulk Sb in a suitable solvent enables one to produce Sb nanosheets (Fig. S1). The Tyndall effect of the obtained Sb dispersion indicates its colloidal nature. It is worth noting that by employing a cascade centrifugation (CF) protocol, we are able to readily tune the lateral size, thickness, and surface oxygen content of the prepared Sb nanosheets.

The X-ray diffraction (XRD) patterns of Sb nanosheets with varying CF speeds are given in Fig. 1c. It can be seen that the exfoliated Sb nanosheets retain high crystallinity with diffraction peaks characteristic of $\beta$-Sb (JCPDS No. 35–0732). No diffraction peaks from $Sb_2O_3$ were discerned (Fig. S2). Note that the (003) and (006) reflections disappeared for the 2D Sb nanosheets (Fig. S2) [26], indicating occurrence of exfoliation along the *c*-axis to form single and few layers. These results were also confirmed by Raman spectroscopy (Fig. 1d and S3). Two sharp

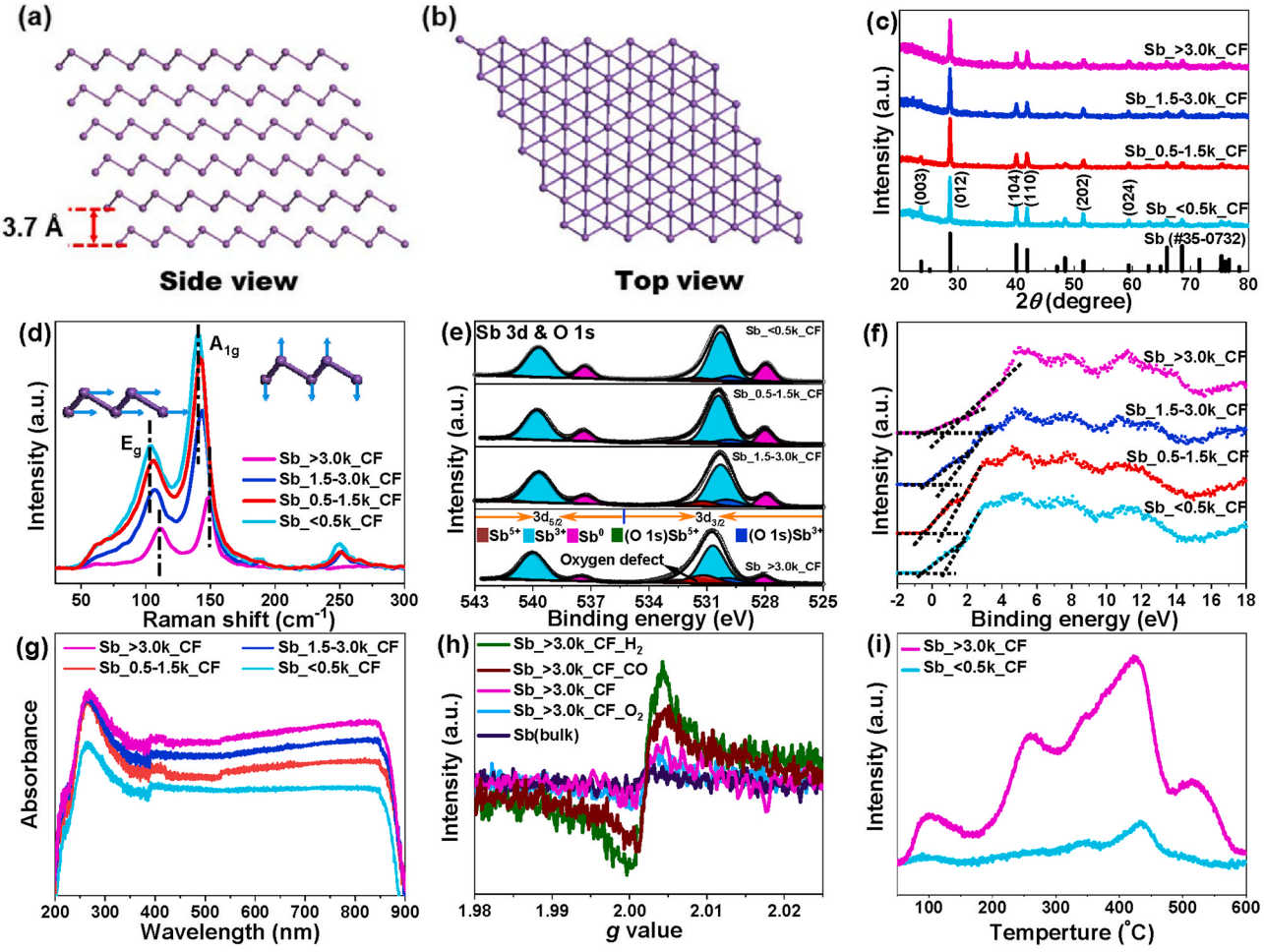


**Fig. 1.** (a) Side view and (b) top view of Sb nanosheet crystal structure. (c) XRD patterns, (d) Raman spectra, (e) deconvoluted Sb 3d and O 1s XPS spectra, (f) valence-band XPS spectra, and (g) UV–Vis diffuse reflectance spectra of the exfoliated Sb nanosheets at different CF speeds. (h) EPR spectra of Sb(bulk), Sb_>3.0k_CF, Sb_>3.0k_CF_$O_2$, Sb_>3.0k_CF_CO, and Sb_>3.0k_CF_$H_2$. (i) $N_2$-TPD profiles of Sb_<0.5k_CF and Sb_>3.0k_CF.

peaks centered at 110.0 and 141.6 $cm^{-1}$ were observed (Fig. 1d), which are ascribed to the $E_g$ and $A_{1g}$ vibration modes of Sb. The two peaks shifted toward higher wavenumbers with an increase of CF speed, which was induced by the decrease of Sb's thickness, in accordance with previous literature on few-layer antimonene [26].

X-ray photoelectron spectroscopy (XPS) measurements were performed to probe the surface composition and chemical state of the obtained Sb nanosheets. Deconvoluted Sb 3d spectra of the Sb nanosheets present three doublets of Sb $3d_{3/2}$ and Sb $3d_{5/2}$ (Fig. 1e and S4). The Sb $3d_{3/2}$ peaks at ~ 528.0, ~ 530.4, and ~ 532.4 eV are attributed to $Sb^0$, $Sb^{3+}$ ($Sb_2O_3$), and $Sb^{5+}$ ($Sb_2O_5$), respectively [26]. This contrasts a predominant Sb $3d_{3/2}$ peak at 530.2 eV for $Sb_2O_3$ (Fig. S5a). The surface Sb oxide fraction increased with decrease of thickness and lateral size as a result of partial oxidation of Sb under ultrasound, which occurs more easily for thinner nanosheets and smaller Sb with more edges [30,31]. Additionally, a positive shift toward higher BEs is observed for the Sb 3d peaks. The O 1s XPS signal which is overlapped with the Sb 3d signal can be resolved into three peaks at 530.2, 529.8, and 531.5 eV, corresponding to oxygen defects [32,33] and lattice oxygen in the respective O–$Sb^{3+}$ and O–$Sb^{5+}$ species [31]. The content of oxygen defects was found to increase with decrease of the thickness and lateral size (Table S1). The valence band (VB) values were determined to be 1.71, 0.77, 0.75, 0.73, and 0.65 V (*vs.* normal hydrogen electrode, NHE) for $Sb_2O_3$ (Fig. S5b) and Sb nanosheets obtained after CF with speed <500 rpm (i.e., Sb_<0.5k_CF), 500–1500 rpm (i.e., Sb_0.5–1.5k_CF), 1500–3000 rpm (i.e., Sb_1.5–3.0k_CF), >3000 rpm (i.e., Sb_>3.0k_CF), respectively (Fig. 1f). Ultraviolet–visible (UV–Vis) diffuse reflectance results show remarkable enhancement of the intensity in the visible region with reduction in Sb's thickness. (Fig. 1g). The band gaps of $Sb_2O_3$ and the Sb nanosheets with different thicknesses and sizes were calculated via the equation $\alpha h\nu = A(h\nu\text{-}E_g)^{1/2}$, where $\alpha$ is absorption coefficient, $h$ is Planck's constant, $f$ is *the* photon frequency, and $A$ is a parameter that depends on transmission probability, and were found to be ~ 4.05 (Fig. S5c), 1.37, 1.39, 1.40, and 1.42 eV (Fig. S6) for commercial $Sb_2O_3$, Sb_<0.5k_CF, Sb_0.5–1.5k_CF, Sb_1.5–3.0k_CF, and Sb_>3.0k_CF, respectively. Notably, the Sb nanosheets exhibit absorption ability in the visible region while $Sb_2O_3$ is only UV-responsive. Further, the corresponding conduction band (CB) values of Sb nanosheets were derived to be −0.60, −0.64, −0.67, and −0.77 eV, which are suitable to potentially facilitate $N_2$ reduction to $NH_3$ in all the cases.

Further electron paramagnetic resonance (EPR) spectroscopy was carried out to analyze trapped electrons in Sb samples (Fig. 1h). Bulk Sb displayed weak EPR signals, indicating extremely low level of defects. In contrast, exfoliated Sb nanosheets exhibited a symmetric pair of peaks with the signal at $g = 2.002$ being attributed to trapped unpaired electrons by oxygen vacancies through adsorbed oxygen species from air ($O^{2-}$) [33]. Strikingly, the EPR signal became much stronger after annealing Sb nanosheets in CO and 8% $H_2$/Ar with the latter being more intense, suggesting a significant increase in oxygen vacancy concentration. As illustrated in Fig. 1i, substantial $N_2$ physisorption at *ca.* 100 °C and chemisorption at 262, 425, and 522 °C are observed over Sb_>3.0k_CF. In sharp contrast, only very weak signals of physi- and chemisorbed $N_2$ on Sb_<0.5k_CF were detected. The high $N_2$ adsorption capacity of Sb_>3.0k_CF definitely offers advantages for photocatalytic $N_2$ reduction.

Aberration corrected high-angle annular dark-field scanning transmission electron microscopy (HAADF-STEM) (Fig. 2a–c) clearly showed flake-like morphology of the exfoliated sample. Energy-dispersive X-ray (EDX) elemental maps (Fig. 2d and e) and the respective EDX spectrum (Fig. S7) indicated that Sb nanosheets were composed of Sb and a small amount of oxygen. The mass fractions of Sb and O atoms were determined to be 98.9 wt% and 1.1 wt%, respectively. The existing oxygen means that the Sb nanosheets were oxidized on the surface. Disordered edges of many nanosheets were observable, as shown in Fig. 2f. High-resolution TEM (HRTEM) images (Fig. 2f–h, and j) along with Fast

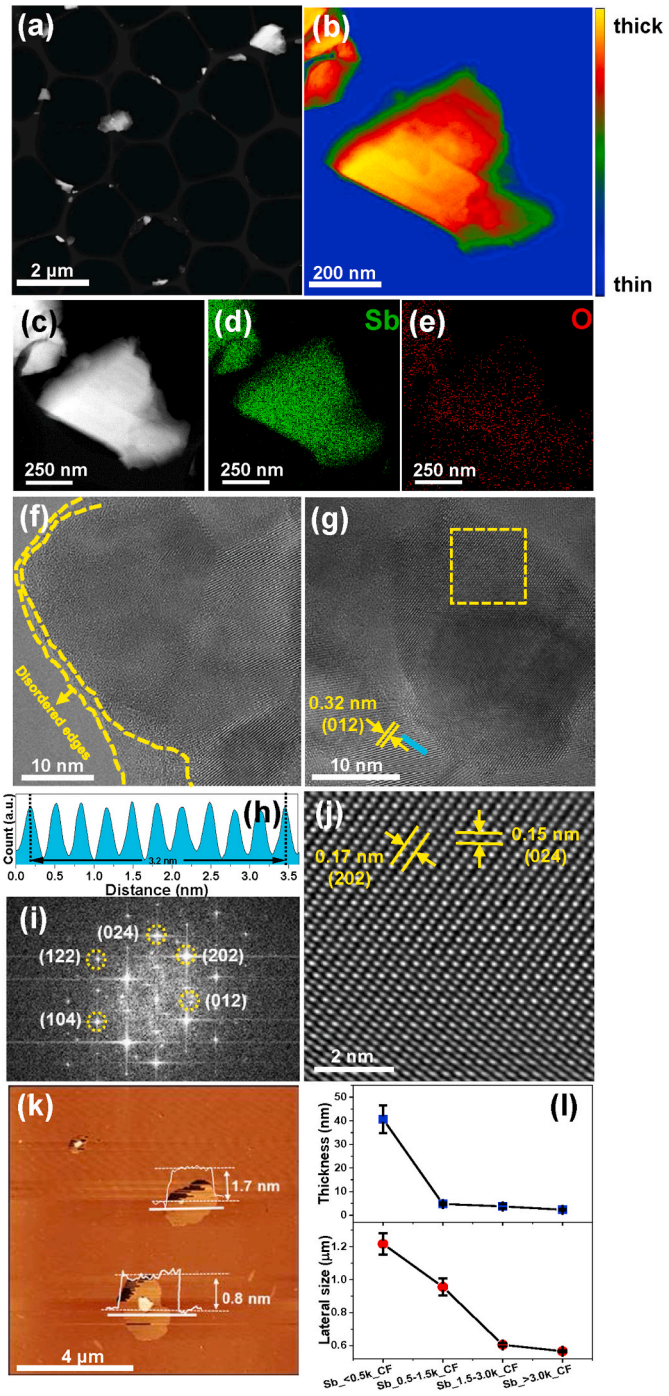


**Fig. 2.** (a) Low-magnification TEM image of exfoliated Sb nanosheets. (b) Quasi-color image of overlapped Sb flakes. (c) HAADF-STEM image of Sb nanosheets and corresponding EDX elemental intensity maps of (d) Sb and (e) O. (f, g) HRTEM image of Sb nanosheets. (h) Profile of the distance of planes denoted by the sky blue line in image (g). (i) FFT and (j) IFFT filtered image of the region enclosed by the square in image (g). (k) Tapping-mode AFM image of Sb_>3.0k_CF deposited on $SiO_2$/Si substrates. (l) Thickness derived by AFM and lateral size estimated by dynamic light scattering (DLS) for Sb nanosheets obtained at varying CF speeds.

Fourier transform (FFT) (Fig. 2i) revealed good crystallinity of the resulting Sb nanosheets, consistent with the aforementioned XRD results.

Atomic force microscopy (AFM) allowed estimation of the thickness of the Sb nanosheets (Fig. 2k and S8). As expected, the average flake thickness decreased with an increase in CF speed, ranging from *ca.* 50

nm at CF < 500 rpm to *ca.* 2 nm at CF > 3000 rpm (top panel in Fig. 2l). The lateral size was found to reduce from 1217 to 566 nm accordingly based on dynamic light scattering (DLS) results (bottom panel in Fig. 2l), while the BET (Brunauer-Emmett-Teller) surface area and single-point total pore volume increased from 2.1 $m^2\ g^{-1}$ to 0.008 $cm^3\ g^{-1}$ to 58.6 $m^2\ g^{-1}$ and 0.151 $cm^3\ g^{-1}$, respectively (Fig. S9 and Table S9).

The 2D Sb nanosheets with tunable thickness and surface defect were examined for photocatalytic $N_2$ (99.999% purity, Fig. S10a) fixation without cocatalysts in water containing methanol using a 300 Xe lamp as the light source. All reduction reactions were carried out continuously for 1 h at about 25 °C. The amount of $NH_3$ generated was determined using the indophenol blue method unless stated otherwise (Fig. S11) [34]. The $NH_3$ yield rates over bulk Sb, $Sb_2O_3$, and the Sb nanosheets with variable sizes are provided in Fig. 3a. Both bulk Sb and $Sb_2O_3$ were shown to be inactive for photochemical $N_2$ reduction. In stark contrast, exfoliated Sb nanosheets substantially enhanced $N_2$ photofixation with remarkable $NH_3$ yield rates. The photocatalytic performance was observed to increase with centrifugation speed, likely a result of more surface oxygen and edge defects of Sb nanosheets due to decrease in thickness and lateral size as reflected by XPS and EPR measurements. Especially, the Sb nanosheets obtained at a CF speed over 3000 rpm afforded the highest $NH_3$ yield rate of 297.5 $\mu g_{NH3}\ h^{-1}\ g_{cat.}^{-1}$ in visible

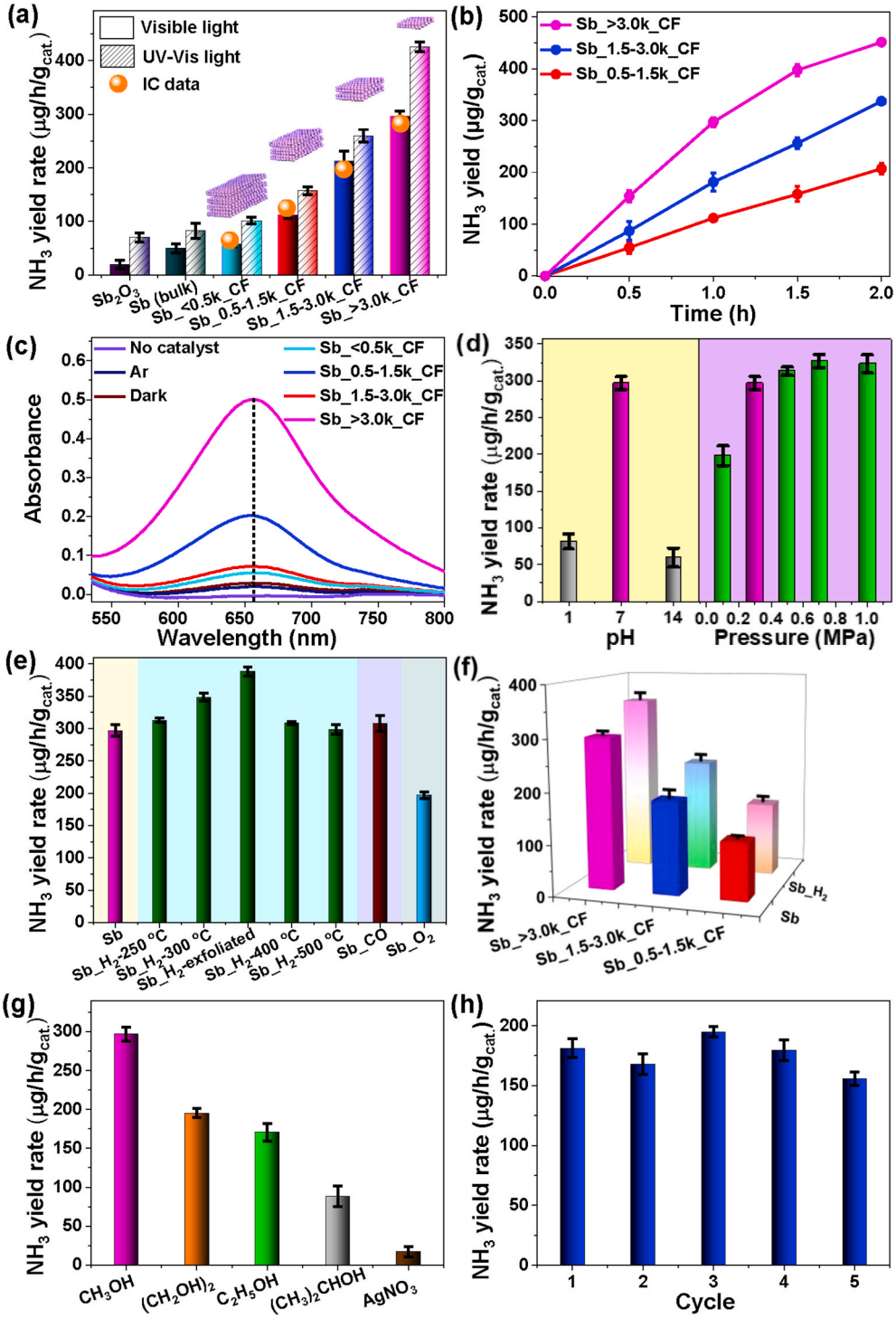


**Fig. 3.** (a) $NH_3$ yield rates under UV–Vis (column with slash) or visible light irradiation (column without slash) determined using the indophenol blue method over Sb nanosheets derived at different CF speeds. The $NH_3$ yield rates under visible light obtained by ion chromatography were also included, as indicated by orange balls (IC data). (b) $NH_3$ yield versus reaction time over the Sb nanosheets. (c) Absorption spectra of Sb nanosheets in the dark, Ar atmosphere (under visible light illumination), visible light, and without catalysts (under visible light illumination). (d) $NH_3$ yield rate of Sb_>3.0k_CF versus pH value (left panel) and pressure (right panel). (e) $NH_3$ yield rates of Sb_>3.0k_CF before and after 1 h of annealing in CO, $O_2$ at 300 °C, or in 8% $H_2$/Ar at 250, 300, 400, and 500 °C. (f) $NH_3$ yield rates of different Sb nanosheets before and after annealing in 8% $H_2$/Ar mixture at 300 °C for 1 h. (g) $NH_3$ yield rates of Sb_>3.0k_CF in methanol, ethylene glycol, ethanol, isopropanol, and $AgNO_3$ trapping agents. (h) $NH_3$ yield rate of Sb_>3.0k_CF against recycling cycle. The yields or yield rates of $NH_3$ displayed in (b) and (d)–(h) were attained under visible light illumination.

light, approximately 6 and 19 times higher than $g$-$C_3N_4$ and amorphous $TiO_2$ under similar reaction conditions [35], respectively. No $N_2H_4$ as by-product was identified by the Watt and Chrisp method, indicating exclusive selectivity for $NH_3$ generation [36]. The evolved $NH_3$ was also quantified by ion chromatography (Fig. S12), which showed similar results with the indophenol blue method (Fig. 3a). Continuous $NH_3$ production was observed over the prepared 2D Sb catalyst (Fig. 3b), showing a quasi-linear relationship between the $NH_3$ yield and illumination time. The turnover frequency (TOF) based on the total moles of Sb in the photocatalyst was calculated to be 0.16 $h^{-1}$. Notably, our catalyst outperforms many previously reported photocatalysts in terms of both $NH_3$ yield rate and TOF (Table S3).

To examine whether there were any interferences, for example ammonia contamination from the environment, the photochemical reactor, or the used nitrogen source, we performed a series of blank and control experiments. Very little $NH_4^+$ was identified by the indophenol blue method in Ar (99.999% purity)-saturated methanol solution (Ar), or without catalyst (No catalyst), or in the dark (Dark) (Fig. 3c). Likewise, no $NH_3$ formation was observed in methanol solutions after exposure to air for 12 h (Fig. S13a), ruling out the effect of possible contamination from the air. The influence of human breath was also excluded by the fact that negligible $NH_4^+$ was detected after the solution was open close to the operator for 1 h (Fig. S13a). To check if trace amounts of impurities in $N_2$ (99.999%) affected the photocatalytic results, a more pure $N_2$ (99.9999%, impurities of $CH_4$ < 0.1 ppm, $O_2$ < 0.1 ppm, $H_2$ < 0.1 ppm, CO < 0.1 ppm, $H_2O$ < 0.5 ppm, and $CO_2$ < 0.1 ppm, Fig. S10b) was used as a feed gas. Similar $NH_3$ yield rates were attained (Fig. S13b). The $N_2$ (99.9999%) was further purified by adsorption with 10 M NaOH solution or alternatively with 1 M $NaClO_2$ solution followed by 10 M NaOH solution to remove any possible $NO_x$ in the feed gas [37]. Almost equivalent $NH_3$ formation rates were obtained (Fig. S13c). These indicate that the minor contaminants in the feed gas did not have an impact on the yield of $NH_3$ here. In addition, we would like to emphasize that no nitrogen-based chemicals were involved during sample preparation, thus avoiding possible interferences that the source of N originated from the catalysts. Moreover, repeated experiments (up to 10 times) showed excellent reproducibility (Fig. S13d), thereby ruling out the effects of contaminations from the environment. These results unambiguously suggest that the detected $NH_3$ was evolved from the reduction of dissolved $N_2$ facilitated by the Sb nanosheet photocatalyst.

As displayed in Fig. 3d, a pH and pressure-dependent effect on $NH_3$ yield was observed, the $N_2$ reduction performance being most optimal (112.2 $\mu g_{NH3}$ $h^{-1}$ $g_{cat.}^{-1}$) at neutral pH (7.0), compared to 81.6 $\mu g_{NH3}$ $h^{-1}$ $g_{cat.}^{-1}$ at acidic pH (1.0) and 59.5 $\mu g_{NH3}$ $h^{-1}$ $g_{cat.}^{-1}$ at basic pH (14.0). Photocatalytic $N_2$ reduction tended to decrease in acidic pH (1.0) due to suppression of water oxidation as a result of increased proton concentration. Although basic pH facilitated water oxidation, the evolution of $NH_3$ was most likely inhibited owing to possible oxidation of the formed $NH_4^+$ [38]. The $NH_3$ yield rate increased after subjecting the Sb nanosheets to annealing in 8% $H_2$/Ar and CO (Fig. 3e and f, and Fig. S14). In particular, the Sb nanosheets annealed in 8% $H_2$/Ar at 300 °C for 1 h presented about 1.2-fold higher $NH_3$ formation rate, reaching up to 348.5 $\mu g_{NH3}$ $h^{-1}$ $g_{cat.}^{-1}$. Such enhancement is mostly likely attributed to increase in surface oxygen vacancy concentration, as reflected by XPS (Fig. S15 and Table S4) and EPR measurements (Fig. 1h). It is noteworthy that the $NH_3$ formation rate can be further improved by controlled exfoliation and separation of the annealed Sb nanosheets in 8% $H_2$/Ar to expose more accessible vacancy sites, approaching 388.5 $\mu g_{NH3}$ $h^{-1}$ $g_{cat.}^{-1}$, almost 8 times that of the bulk counterpart (Fig. 3e). HAADF-STEM and electron energy loss spectroscopy (EELS) analyses indicated the presence of abundant disordered edges and surface oxide defects after annealing in 8% $H_2$/Ar (Fig. S16), which contributed to the outstanding photocatalytic activity. The 2D morphology of the sample was preserved regardless of thermal treatment in different atmospheres (Figs. S16 and S17), however, the production rate of $NH_3$ dropped upon annealing the 2D Sb nanosheet photocatalyst in $O_2$ (Fig. 3e), plausibly due to decrease in oxygen vacancy concentration (Fig. 1h and S15a, and Table S4).

We also investigated the effect of various trapping agents on photocatalytic $NH_3$ production rate over Sb nanosheets, given that their properties can considerably affect the electron transfer kinetics. Of the investigated alcohols that included methanol, ethanol, isopropanol, and ethylene glycol (Fig. 3g and S11f-g), methanol was observed to exhibit the highest enhancement of $NH_3$ yield rate, which may be due to its comparatively small molecule size enabling it to easily approach the catalyst surface [39]. The other alcohols with stronger polarity facilitated higher $NH_3$ formation rates (Table S5) [40]. We also found that addition of $AgNO_3$, an electron scavenger, drastically suppressed the $N_2$ reduction activity, highlighting that electrons are essential to trigger this reaction. Alternatively, when an aprotic solvent $CH_3CN$ was used instead of water, marginal $NH_3$ was generated. This underlines the fact that the protons for $NH_3$ formation stem from water (Table S6). Notably, the defective 2D Sb nanosheets maintained good reusability and stability without apparent deterioration in activity after five cycles (Fig. 3h). Post characterization of the recycled sample by XRD, XPS, VB-XPS, and EPR spectroscopy showed excellent preservation of the photocatalyst structure (Figs. S18 and S19), further confirming the photocatalytic stability of the system.

Electrochemical impedance spectroscopy (EIS) measurements revealed that both internal resistance ($R_s$) and charge transfer resistance ($R_{ct}$) followed the trend Sb_>3.0k_CF < Sb_1.5–3.0k_CF < Sb_0.5–1.5k_CF < Sb_<0.5k_CF < $Sb_2O_3$ (Figs. S20a and b). The fact that the Sb_>3.0k_CF sample showed the smallest impedance indicates that it facilitates the fastest charge transfer and highest ion migration efficiency. The photocurrent transient response was further measured to probe the density of photoinduced charge carriers under irradiation (Fig. 4a). Sb_<0.5k_CF exhibited the weakest signal resulting from its poor activation by the visible light. The Sb_>3.0k_CF sample delivered the highest photocurrent, correlating well with its lowest charge transfer resistance observed in Fig. S20b. This clearly demonstrates the advantages of reducing the Sb nanosheet thickness and introduction of Sb vacancies in photocatalytic $N_2$ fixation [26]. To explore the separation efficiency of photoexcited charge carriers, time-resolved photoluminescence (TRPL) analysis was performed. The average PL lifetime of Sb_>3.0k_CF, Sb_1.5–3.0k_CF, Sb_0.5–1.5k_CF, and Sb_<0.5k_CF at 298 K was estimated to be 17.04, 11.89, 10.01, and 8.46 ns, respectively (Fig. S20c and Table S7). This implies that Sb_>3.0k_CF can offer more free charges to catalyze surface redox reactions. As manifested by PL spectroscopy, Sb_>3.0k_CF provided the weakest emission (Fig. 4b), implying that it possesses the lowest recombination rate of the photogenerated charges. As a consequence, enhancement in charge carrier migration and separation over defective Sb nanosheets contributed to boosted photocatalytic $N_2$ reduction.

From the band structure, the exfoliated 2D Sb nanosheets evidently exhibited sufficient driving force to trigger $N_2$ reduction because the CB minimum is located above the potentials for $N_2$ reduction couples ($N_2$/$NH_3$ at −0.05 V and $N_2$/$NH_4^+$ at 0.273 V *vs.* NHE). In particular, Sb_>3.0k_CF showed the most favourable property for reducing $N_2$ because of its more negative conduction band potential (Fig. 1f and S4). The exact mechanism on visible-light activation of $N_2$ by 2D Sb nanosheets remains elusive. Nonetheless, it is highly probable that electron-hole pairs must have been generated and migrated to the surface of the Sb nanosheets under visible light irradiation, as illustrated in Fig. 4c. The photoexcited electrons are then rapidly transferred to the CB of Sb nanosheets through the interface where they react with $N_2$ to form $NH_3$. The photogenerated holes are expected to be consumed by the sacrificial agent ($CH_3OH$). In addition, $N_2$ chemical adsorption could be greatly facilitated by introduction of surface (Sb and oxygen) vacancies, as has been verified by $N_2$-TPD measurements (Fig. 1i). Effective $N_2$ activation and reduction to $NH_3$ should therefore have been accomplished by these cooperative effects.

To unveil the possible origin of enhanced catalytic activity for $N_2$

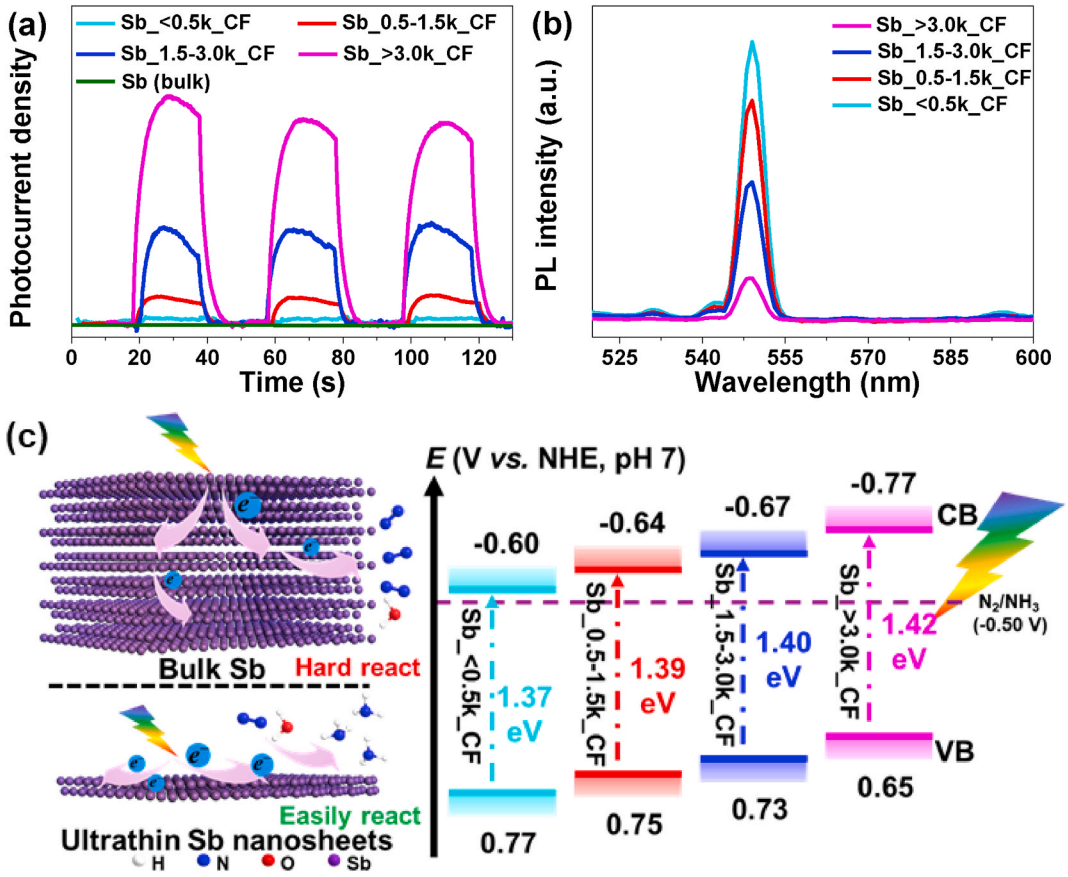


**Fig. 4.** (a) Photocurrent response of Sb_>3.0k_CF recorded under an Ar atmosphere. (b) PL spectra of various Sb nanosheets. (c) Schematic illustration of photocatalytic $N_2$ fixation and the energy band structures of Sb nanosheets.

fixation over Sb nanosheets, DFT calculations were further performed. Based on the XRD results of the as-obtained Sb nanosheets (Fig. 1c), we used a corresponding $\beta$-Sb crystal for modelling. The (001) and (100) facets are considered to construct the basal 2D plane and edge plane of the Sb nanosheets, respectively. XPS disclosed that the surface of the Sb nanosheets consisted of Sb and antimony oxide ($Sb_xO_y$) (Fig. 1e). Given the identification of $Sb^{3+}$ by XPS, we in addition considered crystalline $Sb_2O_3$ facet for modelling $Sb_xO_y$ contents, assuming that the local geometries of $Sb_xO_y$ contents are akin to crystalline $Sb_2O_3$. The (001) facet of $Sb_2O_3$ with orthorhombic *Pccn* space group, the most stable crystalline structure of $Sb_2O_3$ as revealed by the Materials Project database [41], was modelled. Further, we calculated the effect of defect sites on catalytic activity since the $NH_3$ yield rates increased with the defect contents (Fig. 3e). The Sb vacancy ($V_{Sb}$) in Sb(001), $V_{Sb}$ in Sb(100), and O vacancy ($V_O$) in $Sb_2O_3$(001), denoted as $V_{Sb}$(001), $V_{Sb}$(100), and $V_O$-$Sb_2O_3$, respectively, are modelled. Shown in Fig. 5a and b are the optimized geometries of calculation models and reaction intermediates, respectively.

Many previous theoretical studies on $N_2$ reduction have shown that the formation of *NNH ($N_2 + (H^+ + e^-) \rightarrow$ *NNH, where * denotes adsorption site) is generally the most free energy demanding step [42–44]. The stability of *NNH is thus a good descriptor for evaluating $N_2$ reduction catalytic activity. As such, we compared the binding free energy of *NNH ($\Delta G$ (*NNH)) obtained by $G$ (*NNH) – $G$ ($N_2$(g)) – $G$ ($H^+ + e^-$), on various sites in Sb and $Sb_2O_3$. The $\Delta G$ (*NNH) on Sb(001), Sb (100), and $Sb_2O_3$(001) are 2.55, 2.26, and 2.44 eV, respectively (Fig. 5c). This result indicates that the edge sites of Sb nanosheets possess higher catalytic activity than the basal planes.

Interestingly, the $\Delta G$ (*NNH) on $V_{Sb}$(001) (1.66 eV), $V_{Sb}$(100) (1.94 eV), and $V_O$-$Sb_2O_3$ (1.57 eV) are markedly decreased compared to that on pristine Sb and $Sb_2O_3$ (2.26–2.55 eV). This suggests that such defect sites in basal planes and edge sites can greatly facilitate *NNH formation. The theoretical results are consistent with the catalytic activity trends obtained experimentally, indicating that Sb and O vacancy sites in Sb nanosheets play a major role in $N_2$ fixation.

## 3. Conclusions

In summary, we have demonstrated for the first time highly efficient visible light-driven $N_2$ reduction to $NH_3$ by ultrathin 2D Sb nanosheets at ambient conditions. Synergistically tuning the thickness and surface defect sites of the 2D nanostructure allowed remarkable enhancement of its photocatalytic performance. The $NH_3$ yield rate delivered by the defective 2D photocatalyst was as high as 388.5 $\mu g_{NH3}$ $h^{-1}$ $g_{cat.}^{-1}$ under visible light illumination, considerably outperforming bulk Sb and $Sb_2O_3$. By combining experiments and DFT calculations, we believe that the unexpectedly high activity of the 2D Sb is mainly attributed to abundant exposed surface catalytic sites associated with atomic thickness and a large density of active surface defects, which greatly promoted charge carrier migration and separation. Our approach may also be potentially extended to activate other 2D element systems for high-performance and sustainable $NH_3$ production.

## 4. Experimental

### 4.1. Reagents and materials

All chemicals involved in this work were of analytical grade and used without further treatments. Bulk antimony was bought from Nanjing MKNANO Tech. Co., Ltd. (www.mukenano.com). Commercial $Sb_2O_3$, $NH_4Cl$, and NaOH were obtained from Aladdin. Isopropanol (IPA), methanol, ethanol, ethylene glycol, and $CH_3CN$ were provided by

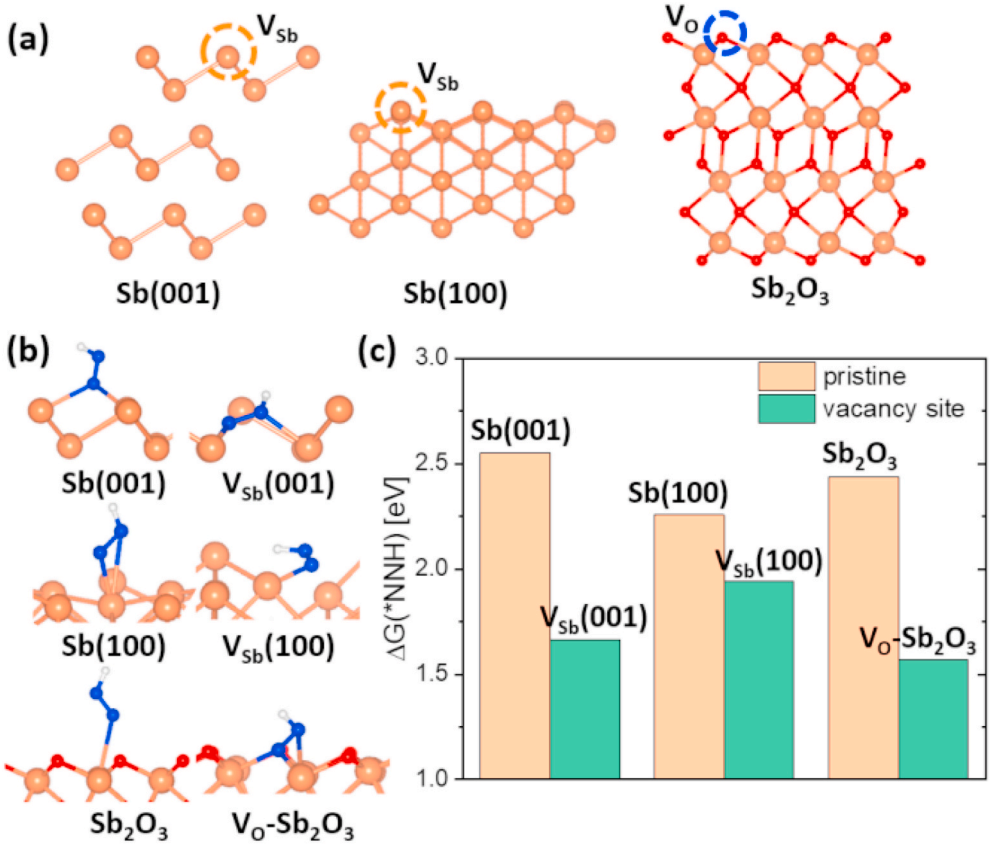


**Fig. 5.** (a) Side-view of the Sb(001), Sb(100), and $Sb_2O_3$. $V_{sb}$, and $V_O$ sites are represented in the dashed circles. (b) The optimized geometries of *NNH. The orange, red, blue, and white balls denote Sb, O, N, and H atoms, respectively. (c) The calculated $\Delta G$ (*NNH) on Sb(001), $V_{Sb}$(001), Sb(100), $V_{Sb}$(100), $Sb_2O_3$, and $V_O$-$Sb_2O_3$ in eV.

Aldrich. $^{14}N_2$ gas (99.999% purity) and argon gas (99.999% purity) were supplied by Beijing Haipu Gas Co., Ltd (http://151999.71ab.com/). $^{14}N_2$ gas (99.9999% purity) was purchased from Hycegas Co., Ltd (http://www.hycegas.com/).

### 4.2. Synthesis of 2D antimony (Sb nanosheets)

Bulk antimony was smashed into powder in a mortar. Then the powder was dispersed in 400 mL of isopropanol (IPA) and ultrasonicated for 20 h at room temperature. The suspension containing different layers of Sb nanosheets was centrifuged at different centrifugation (CF) speeds for 10 min. The resultant Sb nanosheets were collected by filtering and drying at 60 °C overnight, and marked as Sb_<0.5k_CF (the sediment after CF at 500 rpm), Sb_0.5–1.5k_CF [the sediment after CF of the supernatant (obtained after CF at 500 rpm) at 1500 rpm], Sb_1.5–3.0k_CF [the sediment after CF of the supernatant (obtained after CF at 1500 rpm) at 3000 rpm], and Sb_>3.0k_CF (filtered from the supernatant obtained after CF at 3000 rpm), respectively.

### 4.3. Electrochemical measurements

The electrochemical analysis was performed via a CHI 660D electrochemical workstation (Shanghai Chenhua, China) using a standard three-electrode quartz cell. An Xe lamp (MerryChange MC-X301) was used as a light source. To make a working electrode, catalyst powder was deposited on an indium tin oxide (ITO) substrate by Nafion coating. In brief, 1.2 mg of a catalyst was suspended in 200 μL of IPA/$H_2O$ solution (volume ratio of 1:1) and 1 μL of 5% Nafion solution, and the mixture was ultrasonically dispersed for 60 min. Then, the obtained slurry was coated on the ITO glass. After evaporation of IPA, the catalyst-coated ITO substrate was used as a working electrode. During electrochemical impedance and photocurrent measurements, the electrolyte was a 0.5 M $Na_2SO_4$ solution that was saturated with Ar.

### 4.4. Photocatalytic tests

Photocatalytic $N_2$ fixation was carried out in a cylindrical stainless-steel reactor with a quartz window having a diameter of 2.5 cm on the top. In brief, 5 mL of aqueous solution containing 20% methanol (a photogenerated hole scavenger) and 1 mg catalyst were transferred into the reactor. The reactor was charged with 0.3 MPa of $N_2$ after removal of the air by degassing under vacuum for three times. Then, the reactor was sealed and irradiated under UV–Vis or simulated visible light (with a cut off filter, $\lambda \geq 420$ nm) using a 300 W Xenon lamp. After reaction, the gas was released by bubbling into a tail gas absorber containing 10 mL of 0.1 M HCl solution. The amount of $NH_4^+$ in the resultant solution was analyzed by the indophenol blue method. Liquid products in the reactor were centrifuged to remove the catalyst and probed by using the indophenol blue method. The yield of $NH_3$ was calculated based on the combination of the two detected values.

To test reusability of the catalyst, the used catalyst was recovered by centrifugation after reaction, and washed with distilled water for 3 times and then reused for the next run after drying at 60 °C overnight.

The concentration of $NH_4^+$ was identified by using the indophenol blue method. Specifically, 2 mL of 1 M NaOH solution with 5 wt% of salicylic acid, 1 mL of 0.05 M NaClO, and 0.2 mL of 1 wt% Na [Fe(NO)$(CN)_5$] aqueous solutions were homogeneously mixed. The absorption spectrum of the resulting solution was recorded using a PERSEE UV–Vis spectrophotometer after standing for 2 h. The absorbance at the wavelength of 655 nm was used to determine the concentration. Calibrations of this method in 20% alcohol solutions and 0.1 M HCl solutions were conducted with corresponding standard ammonium chloride solutions

(Fig. S11).

Before ion chromatography measurements, the methanol in solutions was separated by passing through a column. Ion chromatograms of $NH_4Cl$ with different concentrations in water were displayed in Fig. S12a. Based on the standard chromatograms, the quantity of ammonia produced from photocatalytic $N_2$ reduction reaction was determined (Figs. S12b–e).

## Credit author statement

Zhenqing Zhao: designed the experiments, Changhyeok Choi: Formal analysis, performed DFT calculations and analysis, Song Hong: carried out TEM characterization, Huidong Shen: helped in materials synthesis, Chao Yan: conducted AFM and Raman measurements, Justus Masa: assisted with language correction, Yousung Jung: Formal analysis, performed DFT calculations and analysis, Jieshan Qiu: assisted with language correction, Zhenyu Sun: Supervision, Writing - original draft, supervised the entire project and wrote the manuscript. All authors discussed the results

## Declaration of competing interest

The authors declare that they have no known competing financial interests or personal relationships that could have appeared to influence the work reported in this paper.

## Acknowledgment

This work was supported by the National Natural Science Foundation of China (No. 21972010); Beijing Natural Science Foundation (No. 2192039); the State Key Laboratory of Organic-Inorganic Composites (No. oic-201901001); Beijing University of Chemical Technology (XK180301, XK1804-2); and the National Research Foundation of Korea from the Korean Government (NRF-2019M3D1A1079303, NRF-2019M3D3A1A01069099).

## Appendix A. Supplementary data

Supplementary data to this article can be found online at https://doi.org/10.1016/j.nanoen.2020.105368.

## References

[1] S. Wang, X. Hai, X. Ding, K. Chang, Y. Xiang, X. Meng, Z. Yang, H. Chen, J. Ye, Adv. Mater. 29 (2017) 1701774.
[2] M. Zhang, C. Choi, R. Huo, G.H. Gu, S. Hong, C. Yan, S. Xu, A.W. Robertson, J. Qiu, Y. Jung, Z. Sun, Nano Energy 68 (2020) 104323.
[3] J.G. Chen, R.M. Crooks, L.C. Seefeldt, K.L. Bren, R.M. Bullock, M.Y. Darensbourg, P.L. Holland, B. Hoffman, M.J. Janik, A.K. Jones, Science 360 (2018) eaar6611.
[4] H. Tao, C. Choi, L.-X. Ding, Z. Jiang, Z. Han, M. Jia, Q. Fan, Y. Gao, H. Wang, A. W. Robertson, S. Hong, Y. Jung, S. Liu, Z. Sun, Chem 5 (2019) 204.
[5] Q. Wang, Y. Lei, D. Wang, Y. Li, Energy Environ. Sci. 12 (2019) 1730.
[6] C. Guo, J. Ran, A. Vasileff, S. Qiao, Energy Environ. Sci. 11 (2018) 45.
[7] C. Ling, X. Niu, Q. Li, A. Du, J. Wang, J. Am. Chem. Soc. 140 (2018) 14161.
[8] S. Liu, S. Wang, Y. Jiang, Z. Zhao, G. Jiang, Z. Sun, Chem. Eng. J. 373 (2019) 572.
[9] S. Liu, Y. Wang, S. Wang, M. You, Z. Zhao, G. Jiang, J. Qiu, B. Wang, Z. Sun, ACS Sustain. Chem. Eng. 7 (2019) 6813.
[10] R. Shi, Y. Zhao, G.I.N. Waterhouse, S. Zhang, T. Zhang, ACS Catal. 9 (2019) 9739.
[11] J. Di, J. Xia, M.F. Chisholm, J. Zhong, C. Chen, X. Cao, F. Dong, Z. Chi, H. Chen, Y. Weng, J. Xiong, S. Yang, H. Li, Z. Liu, S. Dai, Adv. Mater. 31 (2019) 1807576.
[12] G.N. Schrauzer, T.D. Guth, J. Am. Chem. Soc. 99 (1977) 7189.
[13] H. Jia, A. Du, H. Zhang, J. Yang, R. Jiang, J. Wang, C. Zhang, J. Am. Chem. Soc. 141 (2019) 5083.
[14] T. Hou, Y. Xiao, P. Cui, Y. Huang, X. Tan, X. Zheng, Y. Zou, C. Liu, W. Zhu, S. Liang, L. Wang, Adv. Energy Mater. 9 (2019) 1902319.
[15] J. Yang, Y. Guo, R. Jiang, F. Qin, H. Zhang, W. Lu, J. Wang, J. Yu, J. Am. Chem. Soc. 139 (2018) 8497.
[16] Y. Zhao, Y. Zhao, R. Shi, B. Wang, G.I.N. Waterhouse, L.-Z. Wu, C.-H. Tung, T. Zhang, Adv. Mater. 31 (2019) 1806482.
[17] Z. Sun, N. Talreja, H. Tao, J. Texter, M. Muhler, J. Strunk, J. Chen, Angew. Chem. Int. Ed. 57 (2018) 7610.
[18] Z. Sun, T. Ma, H. Tao, Q. Fan, B. Han, Chem 3 (2017) 560.
[19] Q. Fan, C. Choi, C. Yan, Y. Qu, J. Qiu, S. Hong, Y. Jung, Z. Sun, Chem. Commun. 55 (2019) 4246.
[20] S. Sun, X.M. Li, W. Wang, L. Zhang, X. Sun, Appl. Catal. B Environ. 200 (2017) 323.
[21] R. Feng, W. Lei, G. Liu, M. Liu, Adv. Mater. 30 (2018) 1804770.
[22] H. Li, J. Shang, Z. Ai, L. Zhang, J. Am. Chem. Soc. 137 (2015) 6393.
[23] Y. Zhang, N. Dong, H. Tao, C. Yan, J. Huang, T. Liu, A.W. Robertson, J. Texter, J. Wang, Z. Sun, Chem. Mater. 29 (2017) 6445.
[24] Z. Sun, Y. Zhang, H. Yu, C. Yan, Y. Qu, S. Hong, H. Tao, A.W. Robertson, Z. Wang, A.A. Padua, Nanoscale 10 (2018) 12543.
[25] P. Ares, J.J. Palacios, G. Abellan, J. Gomez-Herrero, F. Zamora, Adv. Mater. 30 (2018) 1703771.
[26] X. Wang, J. He, B. Zhou, Y. Zhang, J. Wu, R. Hu, L. Liu, J. Song, J. Qu, Angew. Chem. Int. Ed. 57 (2018) 8668.
[27] F. Li, M. Xue, J. Li, X. Ma, L. Chen, X. Zhang, D.R. MacFarlane, J. Zhang, Angew. Chem. Int. Ed. 56 (2017) 14718.
[28] H. Tao, Y. Gao, N. Talreja, F. Guo, J. Texter, C. Yan, Z. Sun, J. Mater. Chem. A 5 (2017) 7257.
[29] H. Tao, Y. Zhang, Y. Gao, Z. Sun, C. Yan, J. Texter, Phys. Chem. Chem. Phys. 19 (2017) 921.
[30] J. Wang, D. Feng, W. Wu, M. Zeng, Y. Li, Polym. Degrad. Stabil. 31 (1991) 129.
[31] F. Garbassi, Surf. Interface Anal. 2 (2010) 165.
[32] P. Li, Z. Zhou, Q. Wang, M. Guo, S. Chen, J. Low, R. Long, W. Liu, P. Ding, Y. Wu, Y. Xiong, J. Am. Chem. Soc. (2020), https://doi.org/10.1021/jacs.0c05097.
[33] Z. Han, C. Choi, S. Hong, T. Wu, Y. Soo, Y. Jung, J. Qiu, Z. Sun, Appl. Catal. B Environ. 257 (2019) 117896.
[34] Y. Zhao, R. Shi, X. Bian, C. Zhou, Y. Zhao, S. Zhang, F. Wu, G.I.N. Waterhouse, L.-Z. Wu, C.-H. Tung, T. Zhang, Adv. Sci. 6 (2019) 1802109.
[35] Z. Zhao, S. Hong, C. Yan, C. Choi, Y. Jung, Y. Liu, S. Liu, X. Li, J. Qiu, Z. Sun, Chem. Commun. 55 (2019) 7171.
[36] G.W. Watt, J.D. Chrisp, Anal. Chem. 24 (1952) 2006.
[37] H. Chu, T.-W. Chien, B.W. Twu, J. Hazard Mater. 84 (2001) 241.
[38] H. Hirakawa, M. Hashimoto, Y. Shiraishi, T. Hirai, J. Am. Chem. Soc. 139 (2017) 10929.
[39] W. Chen, A. Chan, Z.H.N. Al-Azri, A.G. Dosado, M.A. Nadeem, D.S. Waterhouse, H. Idriss, G.I.N. Waterhouse, J. Catal. 329 (2015) 499.
[40] Y. Yang, C. Chang, H. Idriss, Appl. Catal. B Environ. 67 (2006) 217.
[41] A. Jain, S.P. Ong, G. Hautier, W. Chen, W.D. Richards, S. Dacek, S. Cholia, D. Gunter, D. Skinner, G. Ceder, Apl. Mater. 1 (2013), 011002.
[42] C. Choi, S. Back, N.-Y. Kim, J. Lim, Y.-H. Kim, Y. Jung, ACS Catal. 8 (2018) 7517.
[43] J.H. Montoya, C. Tsai, A. Vojvodic, J.K. Norskov, ChemSusChem 8 (2015) 2180.
[44] E. Skulason, T. Bligaard, S. Gudmundsdóttir, F. Studt, J. Rossmeisl, F. Abild-Pedersen, T. Vegge, H. Jonsson, J.K. Nørskov, Phys. Chem. Chem. Phys. 14 (2012) 1235.